

Inducing *n*- and *p*-Type Thermoelectricity in Oxide Superlattices by Strain Tuning of Orbital-Selective Transport Resonances

Benjamin Geisler* and Rossitza Pentcheva†

*Department of Physics and Center for Nanointegration (CENIDE), Universität Duisburg-Essen,
Lotharstraße 1, 47057 Duisburg, Germany*



(Received 28 August 2018; revised manuscript received 5 March 2019; published 16 April 2019)

By combining first-principles simulations including an on-site Coulomb-repulsion term and Boltzmann theory, we demonstrate how the interplay of quantum confinement and epitaxial strain allows one to selectively design *n*- and *p*-type thermoelectric response in $(\text{LaNiO}_3)_3/(\text{LaAlO}_3)_1(001)$ superlattices. In particular, varying strain from -4.9% to 2.9% tunes the Ni orbital polarization at the interfaces from -6% to 3% . This is caused by an electron redistribution among Ni $3d_{x^2-y^2}$ - and $3d_{z^2}$ -derived quantum-well states, which respond differently to strain. Owing to this charge transfer, the position of emerging cross-plane-transport resonances can be tuned relative to the Fermi energy. For moderate compressive strains of -1.5% and -2.8% , the cross-plane Seebeck coefficient reaches approximately -60 and $100 \mu\text{V/K}$ at around room temperature, respectively. This provides a compelling mechanism to tailor thermoelectric materials. Finally, we demonstrate the robustness of the proposed concept with respect to oxygen-vacancy formation.

DOI: 10.1103/PhysRevApplied.11.044047

I. INTRODUCTION

Transition-metal oxides are attractive for thermoelectric applications owing to their chemical and thermal stability and environmental friendliness as well as the prominent role of electronic correlations [1,2]. Considerable experimental and computational [3] research aims at finding oxide thermoelectrics with improved performance, mostly among bulk materials by doping [4–7] or strain [8]. An alternative strategy is to exploit heterostructuring and dimensional confinement [9–16]. This is promoted by the advancement of growth techniques that allow the design of transition-metal-oxide superlattices (SLs) with atomic precision [17–24].

One system that has been in the focus of intensive research comprises the correlated metal LaNiO_3 (LNO) and the wide-gap band insulator LaAlO_3 (LAO). Following the initial proposal of Chaloupka and Khaliullin [25], significant effort was concentrated on controlling the degree of Ni e_g orbital polarization, which is absent in bulk LNO. For instance, Wu *et al.* [26] reported an orbital polarization of -3% to 8% in $(\text{LNO})_4/(\text{LAO})_4(001)$ SLs on YAlO_3 , LaSrAlO_4 , and SrTiO_3 (STO). Simulations for ultrathin $(\text{LNO})_1/(\text{LAO})_1(001)$ SLs revealed a similar variation of the orbital polarization between -4% and 2% for LAO and STO substrates [27]. Variation of the spacer

material [26,28] or the crystallographic orientation [29] allows for even higher values.

Several studies have shown that a single or a double LNO layer confined in LAO along the [001] direction undergoes a metal-to-insulator transition (MIT) for tensile strain [19,27,30] and exhibits magnetic order [20,31–33]. The origin of this MIT is, however, not related to orbital polarization, as initially proposed, but to a disproportionation into two inequivalent Ni sites [27]. With increasing LNO thickness, for example, in $(\text{LNO})_n/(\text{LAO})_3(001)$ SLs on STO ($n = 3, 5, 10$) [16,27,30] or $(\text{LNO})_4/(\text{LAO})_4(001)$ SLs on STO [21,34], the metallic behavior of the nickelate is restored.

While the confinement- and strain-induced opening of a small band gap in $(\text{LNO})_1/(\text{LAO})_1(001)$ SLs enhances strongly the thermoelectric response, the thermoelectric performance of $(\text{LNO})_3/(\text{LAO})_3(001)$ SLs was found to be impeded by (i) the two-dimensional metallic nature of the LNO region and (ii) the too-thick insulating LAO spacer layer, which prohibits vertical transport [16]. On the other hand, efficient thermoelectric energy conversion requires both *n*- and *p*-type materials that are structurally and electronically compatible. To this end, the selective control of interfacial-layer stacking was recently proposed as a strategy to achieve *n*- and *p*-type response in polar $(\text{LNO})_3/(\text{STO})_3(001)$ SLs [15]. Designing the thermoelectric response necessitates quantum control over the spectral-transmission-function asymmetry around the Fermi energy [35,36]. However, the distinct

*benjamin.geisler@uni-due.de

†rossitza.pentcheva@uni-due.de

use of transport resonances, which are attractive for thermoelectric applications [37], has been limited to model studies [38,39] and materials realizations are lacking so far.

Here we explore the thermoelectric properties of $(\text{LNO})_3/(\text{LAO})_1(001)$ SLs from first principles. The single LAO spacer layer induces the formation of distinct Ni-derived quantum-well (QW) states, while at the same time permitting electronic transport. This leads to the emergence of sharp cross-plane-transport resonances associated with the $3d_{z^2}$ -derived QW states. Moreover, by use of strain, the orbital polarization and thus the relative position and occupation of $3d_{x^2-y^2}$ - and $3d_{z^2}$ -derived QW states can be tuned. Interestingly, this mechanism allows one to precisely shift the transport resonances relative to the Fermi energy. Thereby, considerable *n*- and *p*-type thermoelectric response can be obtained in one and the same materials combination by moderately varying the control-parameter epitaxial strain between -1.5% and -2.8% . We thus exemplify how to control and optimize the thermoelectric properties of oxide heterostructures by varying the layer thickness, confinement, and epitaxial strain. Furthermore, we show that the mechanism is robust with respect to oxygen-vacancy (V_O) formation. This opens an unexpected area of application for the design of orbital polarization, which is intensively pursued in artificial transition-metal oxides.

II. METHODS

We perform first-principles calculations in the framework of spin-polarized density-functional theory (DFT) [41] as implemented in QUANTUM ESPRESSO [42]. The generalized-gradient approximation is used for the exchange-correlation functional as parametrized by Perdew, Burke, and Ernzerhof [43]. Static correlation effects are considered within DFT with an on-site Coulomb-repulsion term (DFT + U) [44] with $U = 4$ and $J = 0.7$ eV for Ni 3d states, in line with previous work by us and others [15,16,27,40,45,46]. To take octahedral tilts fully into account, 40-atom $\sqrt{2}a \times \sqrt{2}a \times c$ supercells are used to model the $(\text{LNO})_3/(\text{LAO})_1(001)$ SLs. Epitaxial strain is considered by varying the in-plane lattice parameter a from 3.65 to 3.95 Å. The out-of-plane lattice parameter $c(a)$ is optimized in each case (Fig. 1), as are the atomic positions. All structures exhibit an anti-ferrodistortive $a^-a^-c^-$ octahedral-rotation pattern and ferromagnetic order (see Supplemental Material [47]). The Brillouin zone is sampled by an $8 \times 8 \times 4 \vec{k}$ -point grid [48] and 5-mRy smearing [49]. The BoltzTraP code [50] is used to obtain converged energy- and spin-resolved transmission functions $T_\sigma(E)$ in Boltzmann theory (with a denser $64 \times 64 \times 16 \vec{k}$ -point grid) and thermoelectric quantities according to Sivan and Imry [35], an approach we used in previous studies [15,16,36,51,52]; it is described in the Supplemental Material [47].

III. INTERPLAY OF STRUCTURE AND ORBITAL POLARIZATION

Figure 1 shows the optimized $(\text{LNO})_3/(\text{LAO})_1(001)$ SL structures and cell heights $c(a)$ for several in-plane lattice parameters a , modeling the growth on a variety of substrates imposing compressive strain [such as ScAlO_3 (3.60 Å), YAlO_3 (3.716 Å), or LAO

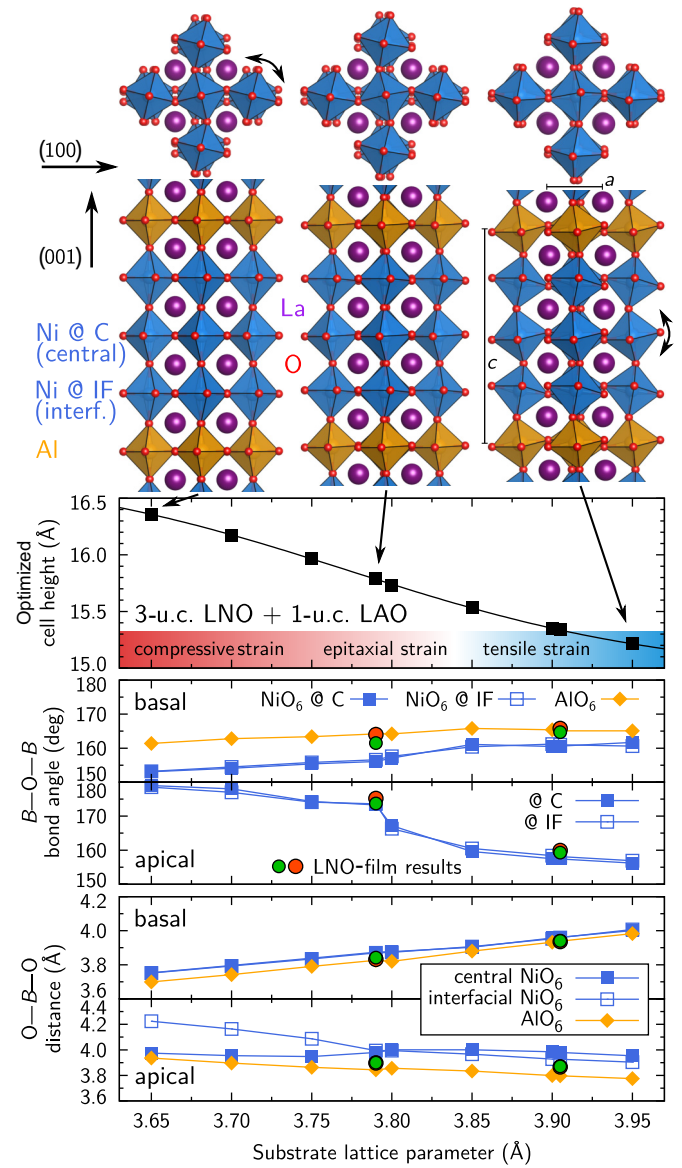


FIG. 1. Top and side views of optimized $(\text{LNO})_3/(\text{LAO})_1(001)$ SLs for $a = 3.65$, 3.79 , and 3.95 Å, ranging from compressive (left) to tensile (right) epitaxial strain. Below them, several optimized $c(a)$ values are shown, together with a fitted curve. Moreover, $B—O—B$ bond angles and $O—B—O$ distances are provided as a function of the substrate lattice parameter a . Green (red) circles mark DFT (XRD) results for bulklike LNO films on LAO and STO [40]. The pseudocubic lattice parameters of LAO, LNO, and STO are 3.79 , 3.838 , and 3.905 Å, respectively. C, central layer; IF, interfacial layer; u.c., unit cell.

(3.79 \AA) or tensile strain [such as STO (3.905 \AA), DyScO₃ (3.94 \AA), or GdScO₃ (3.976 \AA)] [56,57]. The relaxed parameters $c(a)$ for discrete a values are fitted to $c(a) = c_0 \tanh[\tilde{a}(a - a_i)] + c_1$, giving $c_0 = -0.934 \text{ \AA}$, $c_1 = 15.86 \text{ \AA}$, $\tilde{a} = 4.818/\text{\AA}$, and $a_i = 3.773 \text{ \AA}$ (inflection point). With the pseudocubic lattice parameter of LNO, $a_{\text{LNO}} = 3.838 \text{ \AA}$ [40], this corresponds to degrees of epitaxial strain $\epsilon = a/a_{\text{LNO}} - 1$ ranging from -4.9% to 2.9% . The strong octahedral rotations around the c axis present for compressive strain are continuously reduced when shifting to tensile strain. This is reflected in part in the basal B—O—B bond angles, which increase from 153° to 161° (Ni) and from 161° to 165° (Al; 180° implying the absence of any rotation). In contrast, while almost no octahedral rotations around the a axes are present for strong compressive strain, they appear at $a \approx 3.80 \text{ \AA}$, signaled by a sudden decrease of the apical B—O—B bond angles (stronger tilts) from approximately 175° to 165° . This onset is located close to the inflection point a_i of the $c(a)$ curve; the relaxation pattern around this point has been carefully checked to avoid local minima. The basal O—Ni—O and O—Al—O distances increase from 3.7 to 4.0 \AA , whereas the apical O—Al—O and interfacial O—Ni—O distances decrease from 3.95 to 3.78 \AA and from 4.2 to 3.9 \AA , respectively. The central apical O—Ni—O distance is almost constant (approximately 4 \AA). Comparison of the nickelate region with DFT and x-ray-diffraction (XRD) results for 100–200-Å-thick LNO films grown on LAO and STO substrates [40] reveals major similarities (e.g., the strong variation of the apical bond angles with a) (Fig. 1). Similar to the (LNO)₃/(LAO)₃(001) SLs and at variance with the (LNO)₁/(LAO)₁(001) SLs [16], the present system shows no tendency toward an in-plane Ni-site disproportionation and remains metallic for all substrate lattice constants considered.

We quantify the octahedral regularity R and the Ni $3d$ e_g -orbital polarization P (from O—B—O distances d and Ni-orbital occupations n) shown in Fig. 2 by the expressions

$$R = \frac{d_{\text{O—B—O}}^{\text{basal}} - d_{\text{O—B—O}}^{\text{apical}}}{d_{\text{O—B—O}}^{\text{basal}} + d_{\text{O—B—O}}^{\text{apical}}} \quad \text{and}$$

$$P = \frac{n(3d_{x^2-y^2}) - n(3d_z)}{n(3d_{x^2-y^2}) + n(3d_z)}.$$

Positive (negative) values of R denote a compression (elongation) in the [001] direction, while positive (negative) values of P imply a preferential occupation of the in-plane $3d_{x^2-y^2}$ (out-of-plane $3d_z$) orbital. We reduce projection errors arising from the tilts of the octahedra by applying a simple correction scheme to the “Cartesian” orbital occupations (see Supplemental Material [47]). While P is almost constant in the central LNO layer

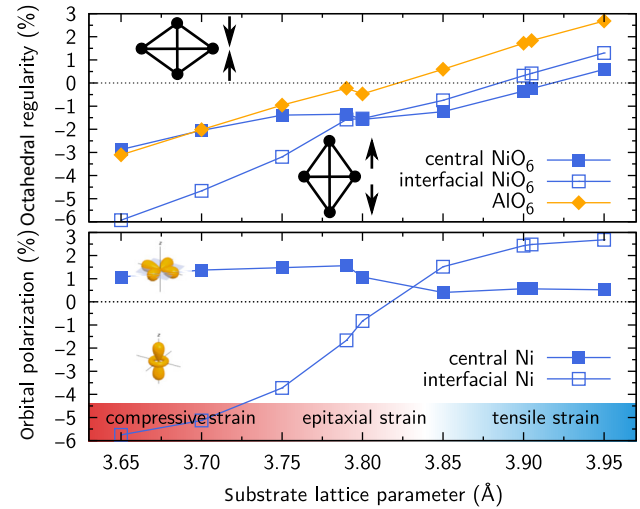


FIG. 2. Regularity R of the NiO₆ and AlO₆ octahedra (upper panel) and Ni $3d$ e_g -orbital polarization P (lower panel) in (LNO)₃/(LAO)₁(001) SLs as a function of a , ranging from compressive (left) to tensile (right) epitaxial strain. Positive (negative) values of R denote a compression (elongation) in the [001] direction, while positive (negative) values of P imply a preferential occupation of the in-plane $3d_{x^2-y^2}$ (out-of-plane $3d_z$) orbital.

(approximately 1%), it changes from -6% (compressive strain) to approximately 3% (tensile strain) in the interfacial LNO layers. Likewise, R of the interfacial NiO₆ octahedra shows the strongest strain dependence and varies between -6% and 1.25% . Experiments on (LNO)₄/(LAO)₄(001) SLs found a similar variation of P with strain [26]. We thus conclude from Fig. 2 that the interfacial Ni-orbital polarization can be designed considerably by strain, displaying the strongest variation around $a = 3.80 \text{ \AA}$.

The evolution of the electronic structure with epitaxial strain is shown exemplarily for $a = 3.70$ and 3.80 \AA in Fig. 3. As previously observed in (LNO)₃/(STO)₃(001) and (LNO)₃/(LAO)₃(001) SLs [15,16], distinct Ni $3d_{x^2-y^2}$ - and $3d_z$ -derived QW states form within the band gap of the spacer material due to confinement. While the $3d_{x^2-y^2}$ -derived QW states are restricted to single LNO layers and show almost no influence of the LAO spacer layer, the $3d_z$ -derived QW states extend over the entire QW and split up strongly. Consequently, the two sets of states have a distinct response to a variation of the substrate lattice parameter: With increasing strain, the $3d_{x^2-y^2}$ -derived ($3d_z$ -derived) QW states are shifted to lower (higher) energies. This impacts the band occupations: Fig. 3 shows that the strong increase of P in the interfacial LNO layers with strain (Fig. 2) is caused by a charge transfer from the localized second $3d_z$ -derived QW state to the set of dispersive $3d_{x^2-y^2}$ -derived QW states. (More information can be found in Supplemental Material [47].)

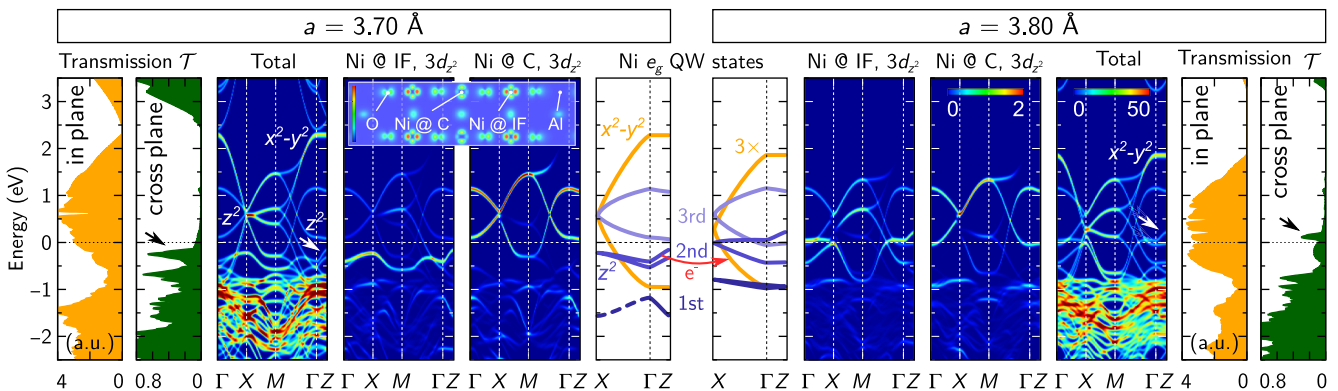


FIG. 3. Majority-spin band structures (total and projections on $3d_{z^2}$ orbitals at different Ni sites) and related electronic transmission $T_\uparrow(E)$ of $(\text{LNO})_3/(\text{LAO})_1(001)$ SLs for two selected substrate lattice parameters, $a = 3.70$ and 3.80 \AA . Note the cross-plane-transmission peak (black arrows) that stems from Ni $3d_{z^2}$ -derived bands along $\Gamma-Z$ (i.e., the second QW state; white arrows) and crosses E_F (zero energy) with increasing epitaxial strain. Analysis of the Ni e_g QW states reveals that the first $3d_{z^2}$ -derived QW state exhibits strong contributions from the central nickelate layer, but is also dispersed below the valence-band maximum of LAO (which is located approximately 0.6 eV below E_F ; see Supplemental Material [47]). The second QW state is clearly localized in the interfacial nickelate layers. The third QW state shows contributions from all nickelate layers, but the contribution from the central layer is strongest. The inset displays the local density of states [53–55] integrated from -0.5 to -0.3 eV below E_F , visualizing predominantly the second QW state. The central panels emphasize schematically the evolution of the different $3d_{x^2-y^2}$ -derived (orange, quasi-threefold-degenerate) and $3d_{z^2}$ -derived (blue) QW states with epitaxial strain. The band structures correspond to k -resolved densities of states, in which each electronic state is represented by a broadened δ distribution of weight 1 (total) or a weight equal to the projection of the respective wave function on $3d_{z^2}$ orbitals at different Ni sites (projected). The color scales are in the unit of reciprocal electronvolts. C, central layer; IF, interfacial layer; a.u., atomic units.

IV. THERMOELECTRIC RESPONSE EXPLOITING TRANSPORT RESONANCES

The single LAO spacer layer allows significant cross-plane electronic transmission (Fig. 3). In particular, resonances emerge, which originate from the $3d_{z^2}$ -derived QW states and whose position can be shifted considerably with respect to the Fermi energy E_F by epitaxial strain. We emphasize that this is possible only due to the opposite response of $3d_{x^2-y^2}$ - and $3d_{z^2}$ -derived QW states to strain, which causes the strong change in orbital polarization (Fig. 2) by a redistribution of electrons (Fig. 3); otherwise, E_F would simply shift with the resonances. Particularly, the cross-plane-transmission peak close to E_F , which stems from Ni $3d_{z^2}$ -derived bands along $\Gamma-Z$ (i.e., the second QW state), shifts from -0.24 to 0.12 eV as a increases from 3.70 to 3.80 \AA . Since the Seebeck coefficient S is highly sensitive to the asymmetry of the transmission around $\mu \sim E_F$, this resonance can be exploited for a targeted design of the thermoelectric response: For 300 K , we find that S ranges between $100 \text{ } \mu\text{V/K}$ ($a = 3.73 \text{ \AA}$, similar to the values for YAlO_3 and GdAlO_3 substrates) and $-60 \text{ } \mu\text{V/K}$ ($a = 3.78 \text{ \AA}$, similar to the values for CeAlO_3 and LAO substrates); at the same time, moderate values are obtained for the electronic figure of merit $ZT|_{\text{el}} = \sigma S^2 T / \kappa_{\text{el}}$, attaining 0.30 and 0.14 (Fig. 4, Table I). Thus, epitaxial strain acts as a control parameter that allows one to induce n -type ($S < 0$) and p -type

($S > 0$) thermoelectric response in one and the same materials combination.

In the constant- (i.e., energy-independent) relaxation-time approximation, S and $ZT|_{\text{el}}$ do not depend on τ .

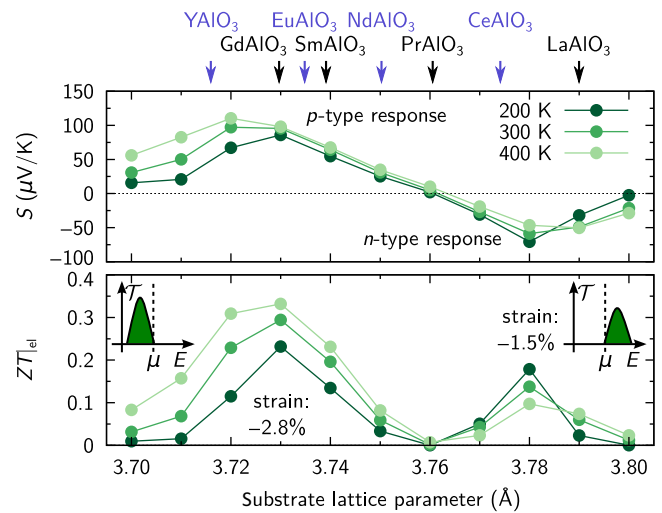


FIG. 4. Thermoelectric properties of $(\text{LNO})_3/(\text{LAO})_1(001)$ SLs at $\mu = E_F$ and three different temperatures for cross-plane transport as a function of a . Epitaxial strain as imposed by exemplary (rare-earth) aluminates substrates is marked (calculated from Ref. [56]). The insets depict the evolution of the transmission peak with strain (cf. Fig. 3).

Since in this work the focus lies on a narrow energy window (around the transmission peak), we consider this approximation to be well justified. Around room temperature, electron-phonon scattering contributes substantially to τ [16] and might also exhibit a strain dependence. While $ZT|_{\text{el}}$ renders the contribution of the electronic system, the phonon heat conductivity κ_{ph} needs to be considered to obtain the total ZT . However, for the SLs studied here, the respective bulk values ($\kappa_{\text{ph}} \sim 0.035 \text{ W/K cm}$ for bulk LNO [58] and approximately 0.1 W/K cm for bulk LAO [59] at 300 K) may not be the relevant quantities; for instance, the presence of interfaces is expected to reduce κ_{ph} due to scattering of phonons.

The thermoelectric performance is higher for the *p*-type case than for the *n*-type case since the intensity of the transmission peak increases from $a = 3.80$ to $a = 3.70 \text{ \AA}$ (Fig. 3) owing to an enhanced dispersion along Γ -Z. The *n*- and *p*-type responses exhibit opposite dependence on temperature: while the former decreases, the latter increases. The system shows strong anisotropy, S being negligible in the plane (not shown here) due to the two-dimensional metallic character (Fig. 3).

Comparison with literature (Table I) reveals that the thermoelectric properties are strongly improved in the $(\text{LNO})_3/(\text{LAO})_1(001)$ SL with respect to bulk LNO and $(\text{LNO})_3/(\text{LAO})_3(001)$ SLs [16] owing to the reduction to a single LAO spacer layer. The system attains S and $ZT|_{\text{el}}$ values that are similar in magnitude to those of metallic $(\text{LNO})_1/(\text{LAO})_1(001)$ SLs at a_{LAO} or $(\text{LNO})_3/(\text{STO})_3(001)$ SLs at a_{STO} [15,16]. Only $(\text{LNO})_1/(\text{LAO})_1(001)$ SLs at a_{STO} , which undergo a MIT for tensile strain [27], show higher values that are

TABLE I. Comparison of the attainable thermoelectric performance of the present system around 300 K (Fig. 4) with related nickelate SLs (DFT + U results) and bulk LNO (i.e., without heterostructuring). (See Supplemental Material [47] for further information.)

$a (\text{\AA})$	$\epsilon (\%)$	$S (\mu\text{V/K})$	$ZT _{\text{el}}$
$(\text{LNO})_3/(\text{LAO})_1(001)$ SL, cross plane (this work)			
3.73	-2.8	100	0.30
3.78	-1.5	-60	0.14
$(\text{LNO})_1/(\text{LAO})_1(001)$ SL, cross plane [16]			
3.79 (a_{LAO})	-1.3	-80	0.2
3.905 (a_{STO})	1.7	± 600	0.8–1.0
$(\text{LNO})_3/(\text{LAO})_3(001)$ SL, cross plane [16]			
3.79 (a_{LAO})	-1.3	-5, 15	< 0.01
3.905 (a_{STO})	1.7	-5, 15	< 0.01
$(\text{LNO})_3/(\text{STO})_3(001)$ SL, cross plane, <i>p</i> -type interfaces [15]			
3.905 (a_{STO})	1.7	135	0.35
LNO bulk (DFT + U , this work)		-12	0.006
LNO bulk (expt. [58], κ_{total})		-18	0.009
LNO bulk (expt. [58], $\kappa_{\text{Wiedemann-Franz}}$)		-18	0.013

comparable to those of the best oxide thermoelectrics [16]. Another beneficial feature of the LAO layers is that they are expected to scatter LNO phonons due to the high mass difference, thereby reducing the detrimental cross-plane lattice thermal conductivity.

V. IMPACT OF OXYGEN VACANCIES

Finally, we explore the robustness of our proposed mechanism with respect to the formation of oxygen vacancies (Fig. 5). To this end, we generate an isolated vacancy in the central LNO layer of our supercell for three substrate lattice constants a , corresponding to a (high) V_{O} concentration of 4.2% of the oxygen sites. We find that the released electrons are accommodated by the $3d_{x^2-y^2}$ -derived QW states, leading effectively to a shift of E_F (Fig. 5). Most importantly, the $3d_{z^2}$ -derived QW states, which give rise to the transport resonances, are preserved. The resonance corresponding to the second QW state crosses E_F at a substrate lattice parameter a of approximately 3.80 \AA instead of approximately 3.76 \AA (cf. Fig. 4). Hence, in the presence of oxygen vacancies, slightly higher strain is required to achieve a selective design of *n*- and *p*-type thermoelectric response as in the case of an ideal SL. The vacancy formation energies under oxygen-rich conditions can be derived from DFT total energies,

$$E_{V_{\text{O}}}^f = E(\text{SL with } V_{\text{O}}) - E(\text{SL, ideal}) + \frac{1}{2}E(\text{O}_2),$$

and amount to $E_{V_{\text{O}}}^f = 2.25, 2.15$, and 2.29 eV for $a = 3.70, 3.80$, and 3.90 \AA , respectively (endothermic). Comparison with the DFT value for bulk LNO of $E_{V_{\text{O}}}^f = 2.8 \pm 0.2 \text{ eV}$

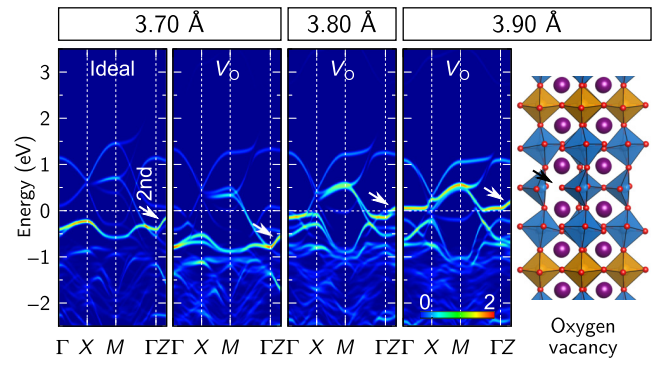


FIG. 5. Impact of oxygen vacancies in $(\text{LNO})_3/(\text{LAO})_1(001)$ SLs at three different substrate lattice constants. The projected majority-spin band structures (interfacial Ni $3d_{z^2}$ orbitals) show that the released electrons are accommodated by the $3d_{x^2-y^2}$ -derived QW states, leading to a shift of E_F (zero energy; cf. Fig. 3), and that the $3d_{z^2}$ -derived QW states, which give rise to the transport resonances, are preserved. The white arrows mark the second QW state, which crosses E_F at approximately 3.80 \AA . On the right, a representative optimized SL geometry at $a = 3.90 \text{ \AA}$ is shown (cf. Fig. 1).

[60] suggests that our SLs are slightly more prone to oxygen-vacancy formation [61].

VI. SUMMARY

By combining density-functional theory calculations with an on-site Coulomb-repulsion term and Boltzmann theory in the constant-relaxation-time approximation, we explored the thermoelectric properties of $(\text{LaNiO}_3)_3/(\text{LaAlO}_3)_1(001)$ superlattices and the impact of different substrate lattice parameters. Variation of epitaxial strain between -4.9% and 2.9% causes an electron redistribution among Ni $3d_{x^2-y^2}$ - and $3d_{z^2}$ -derived quantum-well states that results in a considerable change in the orbital polarization (-6% to 3%). Concomitantly, sharp cross-plane-transport resonances emerging from the $3d_{z^2}$ -derived quantum-well states, induced by the confinement due to the single LaAlO_3 spacer layer, can be shifted relative to the Fermi energy. Slight variation of the control-parameter epitaxial strain between -1.5% and -2.8% is sufficient to selectively induce a considerable n - and p -type thermoelectric response (approximately -60 and $100 \mu\text{V/K}$) in one and the same oxide superlattice. We showed that oxygen vacancies cause only a small shift of this crossover point. This constitutes an interesting mechanism to design thermoelectricity and a concrete materials realization in an oxide system of current interest that calls for further experimental and theoretical exploration. We expect that the results can be extended to a broader class of oxide heterostructures.

ACKNOWLEDGMENTS

This work was supported by the German Research Foundation (Deutsche Forschungsgemeinschaft, DFG) within the SFB/TRR 80 (Projektnummer 107745057), Projects No. G3 and No. G8. Computing time was granted by the Center for Computational Sciences and Simulation of the University of Duisburg-Essen (DFG Grants No. INST 20876/209-1 FUGG and No. INST 20876/243-1 FUGG).

- [1] J. He, Y. Liu, and R. Funahashi, Oxide thermoelectrics: The challenges, progress, and outlook, *J. Mater. Res.* **26**, 1762 (2011).
- [2] S. Hébert and A. Maignan, in *Functional Oxides*, edited by D. W. Bruce, D. O'Hare, and R. I. Walton (John Wiley & Sons, Ltd., Chichester, UK, 2010).
- [3] P. Gorai, V. Stevanovic, and E. Toberer, Computationally guided discovery of thermoelectric materials, *Nat. Rev. Mater.* **2**, 17053 (2017).
- [4] G. Xing, J. Sun, K. P. Ong, X. Fan, W. Zheng, and D. J. Singh, Perspective: n -type oxide thermoelectrics via visual search strategies, *APL Mater.* **4**, 053201 (2016).

- [5] K. F. Garrity, First-principles search for n -type oxide, nitride, and sulfide thermoelectrics, *Phys. Rev. B* **94**, 045122 (2016).
- [6] L. K. Lamontagne, G. Laurita, M. W. Gaulois, M. Knight, L. Ghadbeigi, T. D. Sparks, M. E. Gruner, R. Pentcheva, C. M. Brown, and R. Seshadri, High thermopower with metallic conductivity in p -type Li-substituted PbPdO_2 , *Chem. Mat.* **28**, 3367 (2016).
- [7] T. Okuda, K. Nakanishi, S. Miyasaka, and Y. Tokura, Large thermoelectric response of metallic perovskites: $\text{Sr}_{1-x}\text{La}_x\text{TiO}_3$ ($0 < x < 0.1$), *Phys. Rev. B* **63**, 113104 (2001).
- [8] M. E. Gruner, U. Eckern, and R. Pentcheva, Impact of strain-induced electronic topological transition on the thermoelectric properties of PtCoO_2 and PdCoO_2 , *Phys. Rev. B* **92**, 235140 (2015).
- [9] J. Mao, Z. Liu, and Z. Ren, Size effect in thermoelectric materials, *npj Quantum Mater.* **1**, 16028 (2016).
- [10] L. D. Hicks and M. S. Dresselhaus, Effect of quantum-well structures on the thermoelectric figure of merit, *Phys. Rev. B* **47**, 12727 (1993).
- [11] A. Filippetti, P. Delugas, M. J. Verstraete, I. Palleggi, A. Gadaleta, D. Marré, D. F. Li, S. Gariglio, and V. Fiorentini, Thermopower in oxide heterostructures: The importance of being multiple-band conductors, *Phys. Rev. B* **86**, 195301 (2012).
- [12] P. Delugas, A. Filippetti, M. J. Verstraete, I. Palleggi, D. Marré, and V. Fiorentini, Doping-induced dimensional crossover and thermopower burst in Nb-doped SrTiO_3 superlattices, *Phys. Rev. B* **88**, 045310 (2013).
- [13] I. Palleggi, F. Telesio, D. Li, A. Fête, S. Gariglio, J.-M. Triscone, A. Filippetti, P. Delugas, V. Fiorentini, and D. Marré, Giant oscillating thermopower at oxide interfaces, *Nat. Commun.* **6**, 6678 (2015).
- [14] D. I. Bilc, C. G. Floare, L. P. Zárbo, S. Garabagiu, S. Lemal, and P. Ghosez, First-principles modeling of SrTiO_3 based oxides for thermoelectric applications, *J. Phys. Chem. C* **120**, 25678 (2016).
- [15] B. Geisler, A. Blanca-Romero, and R. Pentcheva, Design of n - and p -type oxide thermoelectrics in $\text{LaNiO}_3/\text{SrTiO}_3(001)$ superlattices exploiting interface polarity, *Phys. Rev. B* **95**, 125301 (2017).
- [16] B. Geisler and R. Pentcheva, Confinement- and strain-induced enhancement of thermoelectric properties in $\text{LaNiO}_3/\text{LaAlO}_3(001)$ superlattices, *Phys. Rev. Mater.* **2**, 055403 (2018).
- [17] A. Ohtomo, D. A. Muller, J. L. Grazul, and H. Y. Hwang, Artificial charge-modulation in atomic-scale perovskite titanate superlattices, *Nature* **419**, 378 (2002).
- [18] J. Mannhart and D. G. Schlom, Oxide interfaces—an opportunity for electronics, *Science* **327**, 1607 (2010).
- [19] J. W. Freeland, J. Liu, M. Kareev, B. Gray, J. W. Kim, P. Ryan, R. Pentcheva, and J. Chakhalian, Orbital control in strained ultra-thin $\text{LaNiO}_3/\text{LaAlO}_3$ superlattices, *Europhys. Lett.* **96**, 57004 (2011).
- [20] A. V. Boris, Y. Matiks, E. Benckiser, A. Frano, P. Popovich, V. Hinkov, P. Wochner, M. Castro-Colin, E. Detemple, V. K. Malik, C. Bernhard, T. Prokscha, A. Suter, Z. Salman, E. Morenzoni, G. Cristiani, H.-U. Habermeier, and B. Keimer, Dimensionality control of electronic phase transitions in nickel-oxide superlattices, *Science* **332**, 937 (2011).

- [21] E. Benckiser, M. W. Haverkort, S. Brück, E. Goering, S. Macke, A. Frañó, X. Yang, O. K. Andersen, G. Cristiani, H.-U. Habermeier, A. V. Boris, I. Zegkinoglou, P. Wochner, H.-J. Kim, V. Hinkov, and B. Keimer, Orbital reflectometry of oxide heterostructures, *Nat. Mater.* **10**, 189 (2011).
- [22] P. Zubko, S. Gariglio, M. Gabay, P. Ghosez, and J.-M. Triscone, Interface physics in complex oxide heterostructures, *Annu. Rev. Condens. Matter Phys.* **2**, 141 (2011).
- [23] S. Middey, J. Chakhalian, P. Mahadevan, J. Freeland, A. Millis, and D. Sarma, Physics of ultrathin films and heterostructures of rare-earth nickelates, *Annu. Rev. Mater. Res.* **46**, 305 (2016).
- [24] M. Lorenz *et al.*, The 2016 oxide electronic materials and oxide interfaces road map, *J. Phys. D: Appl. Phys.* **49**, 433001 (2016).
- [25] J. Chaloupka and G. Khaliullin, Orbital Order and Possible Superconductivity in LaNiO₃/LaMO₃ Superlattices, *Phys. Rev. Lett.* **100**, 016404 (2008).
- [26] M. Wu, E. Benckiser, M. W. Haverkort, A. Frano, Y. Lu, U. Nwankwo, S. Brück, P. Audehm, E. Goering, S. Macke, V. Hinkov, P. Wochner, G. Christiani, S. Heinze, G. Logvenov, H.-U. Habermeier, and B. Keimer, Strain and composition dependence of orbital polarization in nickel oxide superlattices, *Phys. Rev. B* **88**, 125124 (2013).
- [27] A. Blanca-Romero and R. Pentcheva, Confinement-induced metal-to-insulator transition in strained LaNiO₃/LaAlO₃ superlattices, *Phys. Rev. B* **84**, 195450 (2011).
- [28] M. J. Han, C. A. Marianetti, and A. J. Millis, Chemical control of orbital polarization in artificially structured transition-metal oxides: La₂NiXO₆ ($X = B, Al, Ga, In$) from first principles, *Phys. Rev. B* **82**, 134408 (2010).
- [29] D. Doennig, W. E. Pickett, and R. Pentcheva, Confinement-driven transitions between topological and Mott phases in (LaNiO₃)_{*N*}/(LaAlO₃)_{*M*}(111) superlattices, *Phys. Rev. B* **89**, 121110 (2014).
- [30] J. Liu, S. Okamoto, M. van Veenendaal, M. Kareev, B. Gray, P. Ryan, J. W. Freeland, and J. Chakhalian, Quantum confinement of Mott electrons in ultrathin LaNiO₃/LaAlO₃ superlattices, *Phys. Rev. B* **83**, 161102 (2011).
- [31] A. Frano, E. Schierle, M. W. Haverkort, Y. Lu, M. Wu, S. Blanco-Canosa, U. Nwankwo, A. V. Boris, P. Wochner, G. Cristiani, H. U. Habermeier, G. Logvenov, V. Hinkov, E. Benckiser, E. Weschke, and B. Keimer, Orbital Control of Noncollinear Magnetic Order in Nickel Oxide Heterostructures, *Phys. Rev. Lett.* **111**, 106804 (2013).
- [32] D. Puggioni, A. Filippetti, and V. Fiorentini, Ordering and multiple phase transitions in ultrathin nickelate superlattices, *Phys. Rev. B* **86**, 195132 (2012).
- [33] Y. Lu, A. Frano, M. Bluschke, M. Hepting, S. Macke, J. Strempfer, P. Wochner, G. Cristiani, G. Logvenov, H.-U. Habermeier, M. W. Haverkort, B. Keimer, and E. Benckiser, Quantitative determination of bond order and lattice distortions in nickel oxide heterostructures by resonant x-ray scattering, *Phys. Rev. B* **93**, 165121 (2016).
- [34] H. Park, A. J. Millis, and C. A. Marianetti, Influence of quantum confinement and strain on orbital polarization of four-layer LaNiO₃ superlattices: A DFT + DMFT study, *Phys. Rev. B* **93**, 235109 (2016).
- [35] U. Sivan and Y. Imry, Multichannel Landauer formula for thermoelectric transport with application to thermopower near the mobility edge, *Phys. Rev. B* **33**, 551 (1986).
- [36] B. Geisler and P. Kratzer, Spincaloric properties of epitaxial Co₂MnSi/MgO/Co₂MnSi magnetic tunnel junctions, *Phys. Rev. B* **92**, 144418 (2015).
- [37] G. D. Mahan and J. O. Sofo, The best thermoelectric, *Proc. Natl. Acad. Sci. U. S. A.* **93**, 7436 (1996).
- [38] N. Nakpathomkun, H. Q. Xu, and H. Linke, Thermoelectric efficiency at maximum power in low-dimensional systems, *Phys. Rev. B* **82**, 235428 (2010).
- [39] A. N. Jordan, B. Sothmann, R. Sánchez, and M. Büttiker, Powerful and efficient energy harvester with resonant-tunneling quantum dots, *Phys. Rev. B* **87**, 075312 (2013).
- [40] S. J. May, J.-W. Kim, J. M. Rondinelli, E. Karapetrova, N. A. Spaldin, A. Bhattacharya, and P. J. Ryan, Quantifying octahedral rotations in strained perovskite oxide films, *Phys. Rev. B* **82**, 014110 (2010).
- [41] W. Kohn and L. J. Sham, Self-consistent equations including exchange and correlation effects, *Phys. Rev.* **140**, A1133 (1965).
- [42] P. Giannozzi *et al.*, QUANTUM ESPRESSO: A modular and open-source software project for quantum simulations of materials, *J. Phys.: Condens. Matter* **21**, 395502 (2009).
- [43] J. P. Perdew, K. Burke, and M. Ernzerhof, Generalized Gradient Approximation Made Simple, *Phys. Rev. Lett.* **77**, 3865 (1996).
- [44] V. I. Anisimov, I. V. Solovyev, M. A. Korotin, M. T. Czyżyk, and G. A. Sawatzky, Density-functional theory and NiO photoemission spectra, *Phys. Rev. B* **48**, 16929 (1993).
- [45] H.-S. Kim and M. J. Han, Effect of charge doping on the electronic structure, orbital polarization, and structural distortion in nickelate superlattice, *Phys. Rev. B* **91**, 235102 (2015).
- [46] F. Wrobel, B. Geisler, Y. Wang, G. Christiani, G. Logvenov, M. Bluschke, E. Schierle, P. A. van Aken, B. Keimer, R. Pentcheva, and E. Benckiser, Digital modulation of the nickel valence state in a cuprate-nickelate heterostructure, *Phys. Rev. Materials* **2**, 035001 (2018).
- [47] See Supplemental Material at <http://link.aps.org/supplemental/10.1103/PhysRevApplied.11.044047> for additional structural data as well as further details concerning the electronic structure and thermoelectric response of (LaNiO₃)₃/LaAlO₃(001) superlattices.
- [48] H. J. Monkhorst and J. D. Pack, Special points for Brillouin-zone integrations, *Phys. Rev. B* **13**, 5188 (1976).
- [49] M. Methfessel and A. T. Paxton, High-precision sampling for Brillouin-zone integration in metals, *Phys. Rev. B* **40**, 3616 (1989).
- [50] G. K. H. Madsen and D. J. Singh, BoltzTraP. A code for calculating band-structure dependent quantities, *Comput. Phys. Commun.* **175**, 67 (2006).
- [51] B. Geisler, P. Kratzer, and V. Popescu, Interplay of growth mode and thermally induced spin accumulation in epitaxial Al/Co₂TiSi/Al and Al/Co₂TiGe/Al contacts, *Phys. Rev. B* **89**, 184422 (2014).
- [52] D. Comtesse, B. Geisler, P. Entel, P. Kratzer, and L. Szunyogh, First-principles study of spin-dependent thermoelectric properties of half-metallic Heusler thin films between platinum leads, *Phys. Rev. B* **89**, 094410 (2014).

- [53] B. Geisler and P. Kratzer, Atomic-scale detection of magnetic impurity interactions in bulk semiconductors, *Phys. Rev. B* **92**, 100407(R) (2015).
- [54] B. Geisler and P. Kratzer, Strain stabilization and thickness dependence of magnetism in epitaxial transition metal monosilicide thin films on Si(111), *Phys. Rev. B* **88**, 115433 (2013).
- [55] B. Geisler, P. Kratzer, T. Suzuki, T. Lutz, G. Costantini, and K. Kern, Growth mode and atomic structure of MnSi thin films on Si(111), *Phys. Rev. B* **86**, 115428 (2012).
- [56] *Landolt-Börnstein*, edited by K.-H. Hellwege and A. M. Hellwege, New Series Vol. III/4a (Springer-Verlag, Berlin, Heidelberg, New York, 1970).
- [57] N. L. Ross, High pressure study of ScAlO₃ perovskite, *Phys. Chem. Miner.* **25**, 597 (1998).
- [58] J.-S. Zhou, L. G. Marshall, and J. B. Goodenough, Mass enhancement versus Stoner enhancement in strongly correlated metallic perovskites: LaNiO₃ and LaCuO₃, *Phys. Rev. B* **89**, 245138 (2014).
- [59] W. Schnelle, R. Fischer, and E. Gmelin, Specific heat capacity and thermal conductivity of NdGaO₃ and LaAlO₃ single crystals at low temperatures, *J. Phys. D: Appl. Phys.* **34**, 846 (2001).
- [60] A. Malashevich and S. Ismail-Beigi, First-principles study of oxygen-deficient LaNiO₃ structures, *Phys. Rev. B* **92**, 144102 (2015).
- [61] The well-known overbinding of gas-phase O₂ molecules in DFT [60] necessitates a correction of $E(O_2)$, which we perform so as to reproduce the experimental O₂ binding energy of 5.16 eV.